Frictional properties of olivine at high temperature with applications to the strength and dynamics of the oceanic lithosphere

D. S. H. King[1] and C. Marone[1]

Received 8 June 2012; revised 22 October 2012; accepted 23 October 2012; published 15 December 2012.

[1] Faulting and brittle deformation of mantle rocks occurs in many tectonic settings such as oceanic transform faults, oceanic detachment faults, subduction zones, and continental rifts. However, few data exist that directly explore the frictional properties of peridotite rocks. Improved constraints on the brittle deformation of peridotite is important for a more complete understanding of the rheological properties of the lithosphere. Furthermore, our comparatively detailed understanding of plastic deformation in olivine allows us to explore the possible role of thermally activated intracrystalline deformation mechanisms in macroscopically brittle processes. It has been hypothesized, and some experimental data indicate, that plastic yielding by dislocation glide (low temperature plasticity) determines the direct effect in the rate and state frictional constitutive formulation. Plastic flow may also have important implications for the blunting or necking at asperity contacts that influences the time and/or displacement dependent friction evolution effect and frictional healing. We present results from saw cut experiments on fine grained synthetic olivine fault gouge conducted in a gas-medium deformation apparatus in the temperature range of 400–1000°C with 100 MPa confining pressure. We conducted velocity stepping tests to explore the rate and temperature dependence of sliding stability. We also conducted slide-hold-slide experiments to investigate the time and temperature dependence of fault zone restrengthening (frictional healing). The mechanical data and microstructural observations allow us to explore the role of thermally activated processes in frictional sliding. The data indicate systematic temperature dependenceof rate and state variables that can be attributed to plastic yielding at grain to grain contacts. We explore the implications of such temperature dependent behavior for controlling the base of the seismogenic zone in the oceanic lithosphere, and we seek insight into possible mechanistic models for the interactions between fracture and flow that could lead to improved constraints on the strength of the lithosphere.

Citation: King, D. S. H., and C. Marone (2012), Frictional properties of olivine at high temperature with applications to the strength and dynamics of the oceanic lithosphere, *J. Geophys. Res.*, *117*, B12203, doi:10.1029/2012JB009511.

1. Introduction

[2] Experimental studies of rock deformation, in both the brittle and plastic regimes, are largely motivated by the need for physically meaningful constitutive equations representing material behavior ranging from the scale of individual faults to global tectonics [*Dieterich*, 1979; *Kohlstedt et al.*, 1995; *Marone*, 1998a; *Hirth and Kohlstedt*, 2003]. Such constitutive equations model the material response of a rock to an applied force or imposed rate of deformation. A particularly poorly constrained regime of deformation behavior is the semi-brittle regime, in which brittle fracture and plastic flow act simultaneously and interact with one another.

[3] Within the depth range where the yield stress of brittle fracture is less than that of plastic flow, pressure is the dominant variable controlling rock strength and the upper limit of the stress that can be sustained in the lithosphere can be calculated by Byerlee's law [*Byerlee*, 1978]. As pressure increases deeper in the lithosphere, thermally activated plastic creep mechanisms accommodate deformation, and temperature becomes the dominant variable controlling rock strength (for a given strain rate) [*Brace and Kohlstedt*, 1980]. This framework captures important large-scale patterns in the variation of rock strength with depth. However, as stated by *Brace and Kohlstedt* [1980], the yield envelopes developed through such analysis provide only an upper limit

[1]Department of Geosciences, Pennsylvania State University, University Park, Pennsylvania, USA.

Corresponding author: D. S. H. King, Department of Geosciences, Pennsylvania State University, 510 Deike Bldg., University Park, PA 16802, USA. (dking@psu.edu)

0148-0227/12/2012JB009511

to the strength of the lithosphere. Strain localization and lithologic variation can lead to significant weakening relative to simple yield envelopes.

[4] In order to quantitatively understand the conditions under which strain localization occurs and its effects on rock strength, constitutive equations must capture the set of conditions for which deformation is both stable and unstable. Thus, a focus for unified models of deformation has been to identify conditions for which materials strengthen with increasing velocity or strain rate (and remain stable) and for which materials weaken with increasing velocity (and are unstable) [e.g., *Hobbs et al.*, 1990; *Montesi and Zuber*, 2002]. The rate and state friction (hereafter RSF) constitutive framework [*Dieterich*, 1979; *Ruina*, 1983] [*Marone*, 1998a, and references therein], which applies to frictional sliding or frictional shear, is formulated to capture the transient and steady state response to changes in shearing rate, normal stress, temperature and other variables. RSF behavior has been observed for a wide range of materials and conditions [e.g., *Dieterich*, 1979; *Li et al.*, 2011]. However, the underlying microphysical processes are poorly understood and these laws remain largely empirical. In contrast, the constitutive equations describing fully plastic flow have a well understood microphysical basis, but they are developed primarily for steady state flow and do not provide a full description of transient behavior. As a result, these laws do not provide a means for predicting the conditions under which localized deformation occurs, and thus are not capable of fully describing ductile shear zones and other features commonly observed in the geological record.

[5] Part of the solution to bridging the brittle and ductile constitutive frameworks may lie in understanding the role of thermally activated deformation mechanisms in controlling the deformation of asperity contacts in semi-brittle flow. The interpretation that an Arrhenius activated rate process controlling creep at asperities is the physical basis for the friction direct effect has been presented in several studies [*Heslot et al.*, 1994; *Sleep*, 1997; *Baumberger and Berthoud*, 1999; *Nakatani*, 2001; *Rice et al.*, 2001; *Beeler et al.*, 2007]. Several experimental studies have also found transitions in sliding stability as a function temperature [*Shimamoto*, 1986]. Notably, a common observation appears to be a transition from stable sliding at low temperatures, to unstable sliding at intermediate temperatures, and back to stable sliding at high temperatures. This behavior has been observed in wet granite fault gouge [*Blanpied et al.*, 1995], wet gabbro gouge [*He et al.*, 2007], San Andreas fault gouge [*Tembe et al.*, 2009], ilite-quartz gouge [*den Hartog et al.*, 2012], and in olivine-rich rocks [*Stesky et al.*, 1974; *Stesky*, 1978; *Boettcher et al.*, 2007]. The temperatures of the transitions vary among the different materials, but the common observation suggests that transitions in physical mechanisms as a function of temperature may explain the observed behavior.

[6] An observable proxy for the transition from unstable to stable sliding in Earth's crust is the depth extent of seismicity [e.g., *Marone and Scholz*, 1988; *Scholz*, 1998]. Several studies have demonstrated that the depth distribution of seismicity at oceanic transform faults varies by location as a function of geothermal gradient with the cutoff at 600°C [*Abercrombie and Ekstrom*, 2001]. Similarly, the depth extent of seismicity for oceanic intraplate earthquakes varies as a function of heatflow, and crustal age [*Sibson*, 1984] with the cutoff at the 600–750°C isotherm. These observations suggest that temperature is the dominant variable in controlling the transition from unstable to stable sliding at the base of the seismogenic zone.

[7] Alteration phases, such as serpentine, play a significant role in the dynamics of faulting in the oceanic crust and uppermost mantle [e.g., *Escartin et al.*, 1997, 2001], just as phylosilicates play an important role in a variety of crustal fault zone processes [e.g. *Tenthorey et al.*, 1998; *Bos and Spiers*, 2000; *Niemeijer and Spiers*, 2006; *Tenthorey and Cox*, 2006]. However, the P-T conditions at the base of the seismogenic zone are such that the dominant lithology is likely to be relatively unaltered peridotite. Few data exist for the frictional properties of olivine rich rocks, so additional experimental constraints are valuable. Further, because the plastic creep mechanisms for olivine are well-constrained, it is an ideal material to investigate the interactions between brittle and ductile deformation mechanisms.

[8] The frictional behavior of olivine at elevated temperatures was explored by *Boettcher et al.* [2007]. The authors performed velocity steps to investigate the temperature dependence of the stability parameter *(a-b)* (described in section 2.1). In this study, we seek to expand the data set for frictional sliding of olivine to explore its mechanical response in the context of rate and state friction laws. Similar to *Boettcher et al.* [2007], we use San Carlos olivine and conduct our experiments in a gas-medium deformation apparatus. Unlike *Boettcher et al.* [2007], we use a saw cut geometry in which a thin layer of gouge is deformed between two angled forcing blocks, whereas those authors deformed a cylindrical specimen and allowed deformation to localize during the course of deformation. We explore a narrower range of confining pressure (50–150 MPa, with the majority of the experiments conducted at 100 MPa), but we explore a larger range of temperature (400–600°C).

2. Experimental Procedure

[9] Crushed single crystals of olivine from San Carlos, AZ were sorted to <75 μm by settling the powder in water. In two experiments, powder was packed directly into a copper jacket between two disks of porous alumina with a uniaxial load of ~5 MPa. In all other experiments (the bulk of this study), the olivine powder was placed between two angled and serrated tungsten pistons. Into one of the pistons we drilled a 2-mm diameter hole that aligned with the thermocouple hole in the top alumina and zirconia pistons (Figure 1). Adjacent to the sample, the hole was filled with a small amount of porous alumina cement that acted as a filter to keep the powder in place but allow the pore fluid (air) to drain to atmospheric pressure. To achieve as close as possible to a consistent layer thickness among the different experiment runs, and uniform layer thickness within each sample assembly, a thick slurry was prepared by mixing 1.2 g of powder with 5 mL of deionized water. We do not have a method of directly measuring layer thickness during the experiment, but this mass of powder corresponds to nominally 1 mm thickness for the area of the pistons if completely dense, so we expect that layer thickness starts out slightly thicker than 1 mm. The slurry was carefully applied to one of the pistons and the pistons were nested together inside of a clear plastic sleeve so that the uniformity of layer

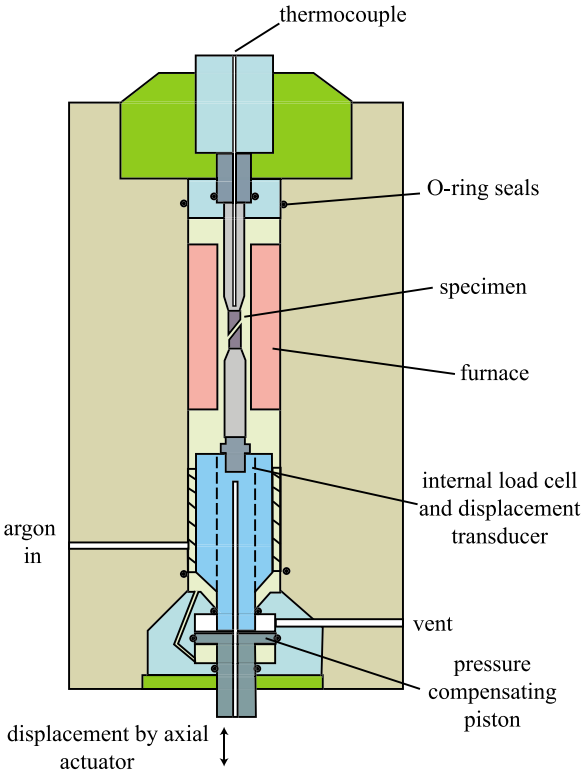

Figure 1. Schematic of gas-medium deformation apparatus [after *Paterson*, 1990].

thickness could be measured and confirmed. The pistons and sample material were then carefully inserted into a copper jacket followed by alumina and zirconia pistons that also fit inside of the copper jacket. The entire assembly was then dried in a vacuum oven for at least 12 hrs. While this drying step thoroughly removed water that was added when creating the slurry, no attempt was made to remove water bound within the olivine lattice structure.

[10] Experiments were conducted in an internally heated, gas-medium deformation apparatus (Figure 1) [*Paterson*, 1990]. Axial displacement was controlled by an actuator mounted below the pressure vessel connected to an electrical servomotor drive. Force was transmitted to the sample through the zirconia and alumina pistons. Both axial displacement and axial load were measured inside the pressure vessel. The main suite of experiments were conducted at temperatures of 400, 600, 800, and 1000°C, with a confining pressure of 100 MPa. An additional set of experiments were run at 600°C at 50 and 150 MPa confining pressure. For the main suite of runs, confining pressure was first raised to ~80 MPa and then pressure and temperature were raised together to the conditions for the experiment. The sample was kept at the hydrostatic pressure of the run conditions for 1 h prior to applying an axial force. In the saw cut experiments, axial displacement was controlled at 1 μm/s for the first 1.2 mm of axial displacement. This displacement was chosen to coincide with the steady state portion of the stress-strain curve (e.g., Figure 2), and thus maximized the displacement range available for velocity step and slide-hold-slide tests.

[11] After samples had reached steady state strength, we conducted velocity-step tests, in which the loading velocity is increased or decreased, and slide-hold-slide tests, in which the actuator is turned off and sliding is ceased for different lengths of time (for details on these methods see Marone:1998p2531). Velocity steps were conducted from 1 to 10 μm/s, 10 to 50 μm/s, and 50 to 1 μm/s. As will be discussed later, the corresponding strain rate for these velocities depends upon the amount of localization in the sample, but estimates for the minimum strain rates are 1.4×10^{-3}, 1.4×10^{-2}, and 7.1×10^{-2} s^{-1} for 1, 10, and 50 μm/s, respectively. At each step, an axial displacement of 300 μm was accommodated. Following the velocity stepping tests, a series of slide-hold-slide tests were performed (Figure 2). These tests were conducted using a background axial displacement rate of 10 μm/s.

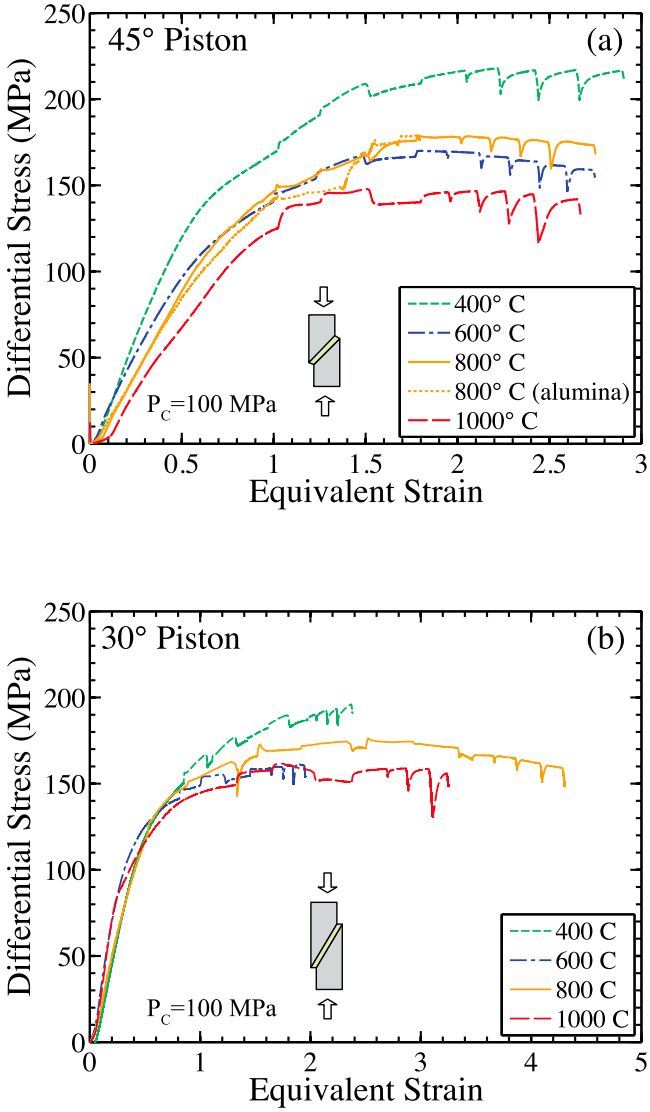

Figure 2. Differential stress versus equivalent strain for samples deformed at four different temperatures at 100 MPa confining pressure (a) with 45° pistons and (b) with 30° pistons. The piston material is tungsten for all of the samples except the dashed line in Figure 2a, which was an alumina piston. Steady state strength is reached at a strain of ~1.5. Variations in stress, beginning at strain of ~1, are due to imposed variations in shearing rate during velocity step tests and slide-hold-slide tests.

After strength had reached a steady value, the actuator was turned off for hold times of 15, 100, 300, and 1000 s. Loading then began again at 10 μm/s and 200 μm of displacement was imposed between each hold. Because the boundary condition for this test is that of constant load point position, if the sample creeps, elastic unloading will occur. The testing apparatus includes several elastic elements (steel end plug, ceramic pistons, and tungsten forcing block) between the actuator and the sliding surface. Consistent with previous works, we found that creep relaxation occurred during the hold periods. Velocity step tests and slide-hold-slide tests were stopped after a maximum axial displacement of ~3.5 mm, which is limited due to the risk of tearing the jacket at greater displacement.

[12] To facilitate comparison of mechanical data with both brittle and ductile deformation experiments, we present results in terms of differential stress and the friction coefficient, μ. We do not correct force measurements for the strength of the jacket because the strength of copper is negligible (<1 MPa) above ~400°CC, as demonstrated in the correction factors for copper jackets developed in *Moore and Lockner* [2008]. For the rate and state modeling, the friction coefficient μ (shear stress τ normalized by the normal stress σ_n) was calculated from the differential stress σ_{dif}, the angle of the gouge layer relative to the axial load ϕ, and the confining pressure P_c according to:

$$\mu = \frac{\tau}{\sigma_n} = \frac{\sigma_{dif}\sin(2\phi)}{2\left(\sigma_{dif}\sin 2(\phi) + P_c\right)}. \quad (1)$$

[13] After deformation, when possible, the gouge layer was carefully removed from the piston. A portion of the sample was placed in a furnace in air at 950°C for ~40 minutes to oxidize the sample and decorate the dislocations [*Kohlstedt et al.*, 1976]. The samples were then vacuum impregnated with a low viscosity epoxy, cut perpendicular to the shear plane and parallel to the shearing direction, and polished using diamond lapping film to a 0.3-μm finish. The polished sections were then examined using a reflected light microscope and a scanning electron microscope (SEM).

2.1. Rate and State Frictional Constitutive Framework

[14] Constitutive equations relating friction μ to sliding velocity V and a state variable θ are powerful tools for applying laboratory results to examine the dynamics of earthquakes and faulting [*Dieterich*, 1979; *Ruina*, 1983]. The rate/state framework has been successful in modeling observed behavior of natural fault systems. However, a major problem associated with these laws is a lack of understanding of the micro-scale physical processes that dictate state variable evolution and frictional sliding behavior. Here, we interrogate the efficacy of the rate/state constitutive laws for our data. We begin by presenting results from a modeling exercise in which best-fit RSF constitutive parameters were determined. In section 4, we discuss the possible physical basis for the parameters. The basic form of these laws [e.g. *Marone*, 1998a] is

$$\mu = \mu_0 + a\ln\left(\frac{V}{V_0}\right) + b\ln\left(\frac{V_0\theta}{D_c}\right) \quad (2)$$

where μ_0 is a constant reference friction for steady state slip at velocity V_0, a and b are empirical constants, and D_c is the critical slip distance. The stability of sliding is determined by the combined parameter $(a - b)$ and elastic, continuum coupling with the surroundings [*Rice and Ruina*, 1983]. If $(a - b) \geq 0$, the material deforms in a stable mode because it strengthens with increasing velocity. If $(a - b) < 0$, material deformation is potentially unstable because it weakens with increasing velocity [*Scholz*, 1998]. Equation (4) must be coupled with an evolution equation for the state variable θ and a description of elastoplastic continuum interactions between frictional processes and the surrounding material. We use a 1D model to describe elastic interactions between the gouge layer and the testing apparatus. For the modeling in our analysis, we use the formulation of *Ruina* [1983]:

$$\frac{d\theta}{dt} = -\frac{V\theta}{D_c}\ln\left(\frac{V\theta}{D_c}\right). \quad (3)$$

This equation emphasizes the dependence of the state variable on slip and sliding velocity, and it may fit more accurately the frictional response to perturbations in slip velocity [*Bayart et al.*, 2006].

3. Results

3.1. Comparison of Sample Geometries

[15] The mechanical data from the two sets of saw cut experiments (45° and 30° pistons) are similar, with both showing a period of stress increase that is independent of temperature, followed by inelastic strain at approximately constant strength (Figure 2). All of the experiments were conducted to approximately the same amount of axial displacement, which translates to similar strain in the samples with 45° pistons in which great care was taken to prepare layers of the same thickness. In the samples deformed with 30° piston, greater variation in sample thickness led to greater variation in the strain experienced by the samples. In general, both sets show similar mechanical responses to imposed shearing. The primary difference is that the samples deformed with a 30° piston reach a steady state differential stress at less displacement (or a lower strain) than the samples deformed with 45° pistons. Presumably, with a 45° piston the sample experiences greater compaction over a longer portion of the displacement, which leads a to a more gradual loading curve.

[16] One concern that arose when conducting the experiments was slight bending at the edges of tungsten pistons at the higher temperatures (800 and 1000°C). The problem was less significant with the 45° pistons in which the thickness of the tapered end of the piston was greater, but still occurred to some extent. To evaluate if this bending contributed significantly to the mechanical data, an experiment was conducted at 800°C using alumina pistons cut at 45° with the surfaces serrated using a saw blade, as for the tungsten pistons. The results from this experiment, plotted as the dashed line in Figure 2a, reveal both a similar magnitude of stress and a similar mechanical response to velocity steps. This similarity with the two different piston materials suggests that it is appropriate to interpret the mechanical results as reflective of the strength of the sample material.

3.2. Effects of Temperature on Strength and Friction

[17] In both sets of saw cut experiments (45° and 30° pistons), shear strength decreases with increasing temperature

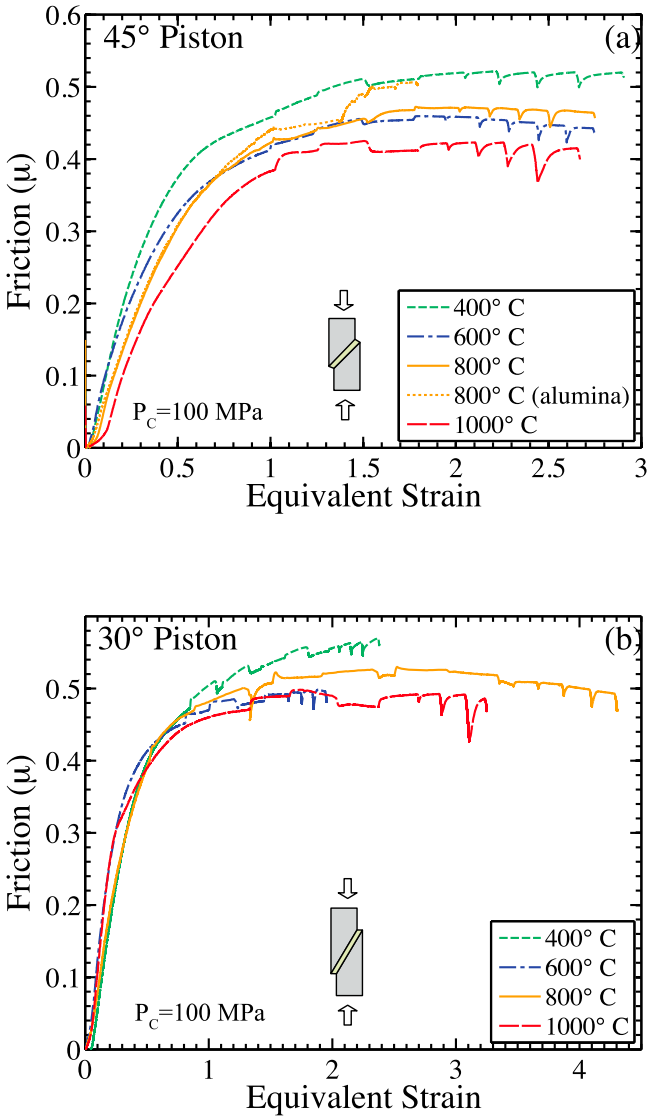

Figure 3. Friction coefficient (calculated from equation (1)) is plotted versus equivalent strain for samples deformed at four different temperatures at 100 MPa confining pressure (a) with 45° pistons and (b) with 30° pistons. The piston material is tungsten for all of the samples except the dashed line in Figure 3a, which was an alumina piston. Steady state strength is reached at a strain of ~1.5. Variations in stress, beginning at strain of ~1, are due to imposed variations in shearing rate during velocity step tests and slide-hold-slide tests.

with the exception of the reversal of the samples deformed at 600 and 800°C (Figure 2). Particularly in the experiments with 45° pistons, early in the experiments, the 800°C samples slide at about the same stress, or a slightly lower stress than the 600°C sample. The friction values are similar for the two sliding angles, with both showing a coefficient of sliding friction of 0.45 to 0.5 (Figure 3). Later in the experiment, the 800°C samples continue to strengthen more than the 600°C sample. These results suggest that some strain- or time-dependent strengthening process is active at 800°C that is not significant at lower temperatures. Possible mechanisms are considered in the discussion.

3.3. Effect of Mean Stress

[18] To explore the pressure sensitivity of deformation, experiments were performed at 50, 100 and 150 MPa at 600°C. The mechanical data are plotted in Figure 4. The data show the expected increase in peak stress with increasing pressure. The strength of the lowest pressure experiment (50 MPa) continues to increase with increasing displacement (strain hardens), while the two samples deformed at higher pressure reach a peak stress before weakening with increasing displacement (strain weakening). The strain weakening trend begins after less displacement at 150 MPa than it does at 100 MPa.

3.4. Transient Response of Gouge to Velocity Steps

[19] To explore the mechanical response of the powders to stepwise changes in velocity, a series of velocity steps were performed starting at 1.2 mm of axial displacement. The main purpose of these tests was to explore the temperature and strain rate conditions for which the material behavior is velocity weakening or velocity strengthening. Both sets of experiments with different piston angles result in the same general patterns of stress evolution at the different temperatures that were explored. The tests reveal two transitions between velocity strengthening and velocity weakening behavior. At 400°C, the sample behavior is velocity strengthening for all rate steps. At 600°C, sample behavior is nearly velocity neutral with the evolution closer to velocity weakening in rate steps with greater sliding velocity. At 800°C, all of the rate steps show velocity weakening behavior. At 1000°C, all of the samples respond with velocity strengthening behavior. The mechanical data for the three rate steps in the set of samples with 45° pistons are presented in Figure 5. To compare the data from the four different temperatures, a linear fit was made to the

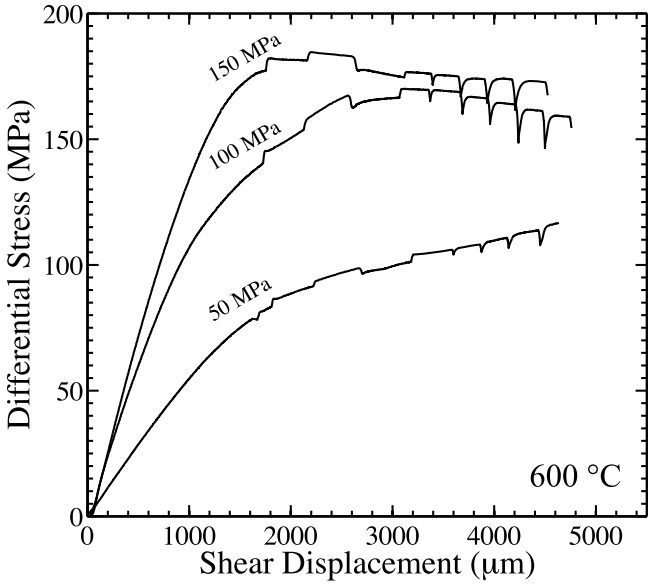

Figure 4. Differential stress versus shear displacement for samples deformed at 600°C at three different confining pressures. Variations in strength are due to imposed variations in shearing rate during velocity step tests and slide-hold-slide tests.

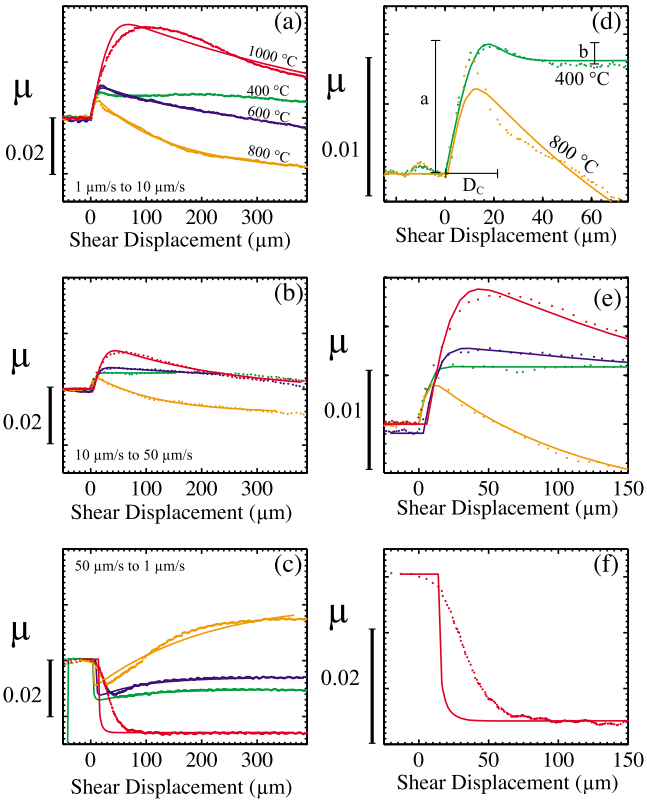

Figure 5. Detail of the friction response for three types of velocity step tests at each temperature. Data are shown as dots. Lines are best-fit rate-state friction models. Figures 5d–5f show detail of selected curves in Figures 5a–5c.Note that friction response for velocity decrease from 50 to 1 μm/s at 1000°C is not fit well.

background strain hardening and removed. The data are presented as the change in μ as a function of displacement (Figure 5).

3.4.1. One State Variable

[20] We modeled friction velocity step tests with the RSF laws in order to explore the direct and transient response to the rate steps in more detail. As described in section 2.1, we used the state variable evolution law of *Ruina* [1983], which emphasizes the role of displacement and contact junction lifetime given by the ratio of D_c to V. In Figures 5a, 5b, and 5c, the data for the three different rate steps are plotted as points and the model fit is plotted as a line. Figure 5 shows data at two scales, to give a better indication of the quality of the fit. In Figure 5d, the approximate magnitudes of a, b, and D_C are indicated graphically for the sample deformed at 400°C. The comparison with the sample deformed at 800°C demonstrates the significant difference in b (evolution parameter) between the two temperatures. Figure 5e presents the first 150 μm of displacement for all of the temperatures analyzed. The model does not fit the data as well for steps down in velocity (Figure 5f). The data consistently have a more gradual drop in μ compared to the model, as indicated in Figure 5f.

[21] Systematic trends in the rate and state parameters with temperature are apparent in the data (Figure 6). In general, all of the rate and state parameters, a, b, and D_c, increase with increasing temperature. The direct effect (a parameter) remains approximately constant at temperatures ranging from 400–800°C, with a significant increase at 1000°C (Figure 6a). The evolution effect (b parameter) increases approximately linearly with increasing temperature with the exception that b for the velocity drop from 50 μm/s to 1 μm/s is essentially zero at 1000°C (Figure 6c). However, as mentioned above, the model has significantly greater misfit in the steps down in velocity, and this is a poorly constrained value. The critical slip distance (D_C) also increases approximately linearly with increasing temperature with significant scatter at 600°C (Figure 6b).

[22] We are able to compare modeled values of a and D_C to those of *Boettcher et al.* [2007] (see their Figure 12). The study of *Boettcher et al.* [2007] modeled only steps down in velocity. Considering the overall trend in D_C observed here (disregarding for the moment the anomalously high values for steps up in velocity at 600°C) the two data sets are in excellent agreement with values ranging from ~50–200. The different behavior for steps up in velocity at 600°C could result from a different process or from changes in the degree of shear localization with velocity [e.g., *Marone and Kilgore*, 1993; *Marone et al.*, 2009]. The values of a in this study are greater than the values in *Boettcher et al.* [2007] by about a factor of two. This could be due to the fact that Boettcher et al. modeled their data with the Dieterich (aging) friction evolution law, whereas we used the Ruina (slip) law, or it could be due in part to differences for velocity increases versus decreases. Particularly at 1000°C, the value of a is lower in the step down in velocity, which is quite close to the value determined in *Boettcher et al.* [2007].

[23] Patterns in the data related to the sliding velocities are also apparent, again with significant scatter. Perhaps most striking is that the samples deformed at 400°C and 800°C have essentially no variation in the rate and state parameters within the range of sliding velocities we explored. The values of the direct effect increase with increasing sliding velocity for the other temperatures.

[24] The direct effect and evolution parameter combine to determine the friction stability parameter (a-b), presented in (Figure 6d). This plot further reveals what can be seen in the raw data (Figure 5a): 1) that the gouge is velocity strengthening for all rate steps at 400°C, 2) it is velocity weakening for all rate steps at 800°C, and 3) it is conditionally weakening for samples deformed at 600 and 1000°C, with velocity weakening behavior more likely with steps up in velocity rather than steps down. The friction parameter ($a - b$) does not appear to vary with sliding velocity for the lowest temperature, but it varies significantly with sliding velocity at higher temperatures.

3.4.2. Two State Variables

[25] We also fit our friction data with a two state variable friction law, to determine if a two-mechanism model is appropriate for interpreting the observed frictional behavior [e.g., *Reinen et al.*, 1992, 1994; *Chester and Higgs*, 1992; *Chester*, 1995].

$$\mu = \mu_0 + a \ln\left(\frac{V}{V_0}\right) + b_1 \ln\left(\frac{V_0\theta}{D_{C1}}\right) + b_2 \ln\left(\frac{V_0\theta}{D_{C2}}\right) \qquad (4)$$

A comparison of the model fits for the rate step from 1 μm/s to 10 μm/s are presented in Figure 7. For the sample deformed at 400°C, the two models fit the data essentially

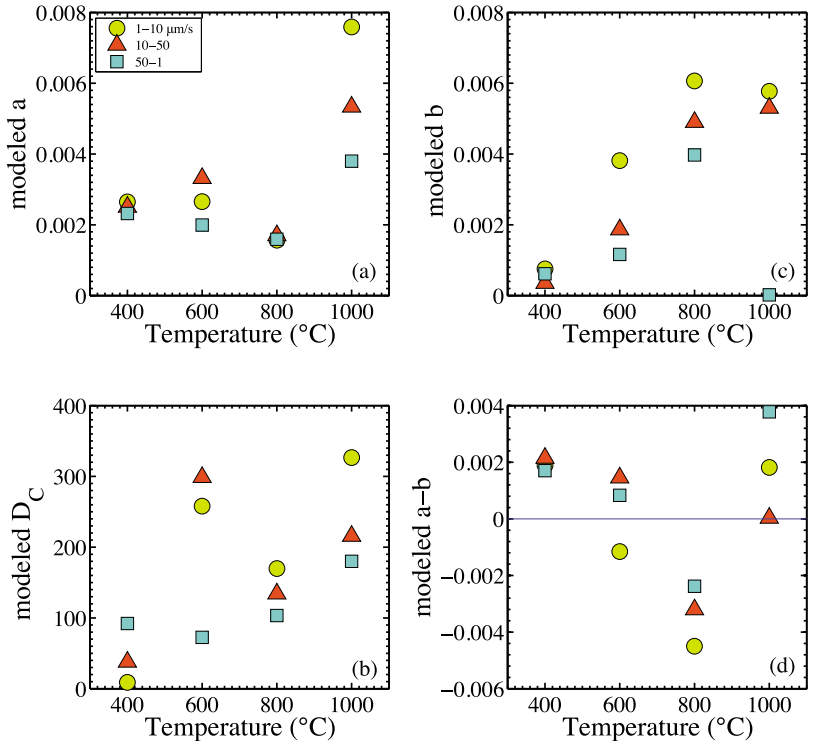

Figure 6. The best-fit rate-state model parameters plotted as a function of temperature. The three different velocity steps are plotted as different symbols. (a) The direct effect, a, is approximately independent of temperature below 800°, but increases between 800 and 1000°C. (b) The critical slip distance D_C increases approximately linearly with increasing temperature. (c) The evolution effect, b, also increases approximately linearly with increasing temperature. (d) The stability parameter, $a - b$, transitions from velocity strengthening to velocity weakening and then back to velocity strengthening with increasing temperature.

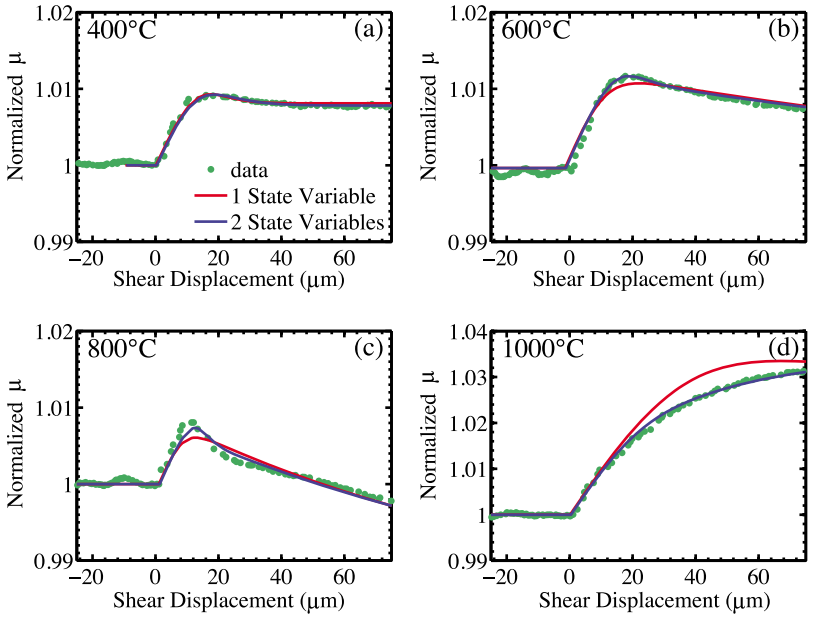

Figure 7. A comparison of the model fit using one and two state variables for the velocity step test from 1 μm/s to 10 μm/s at four different temperatures. At 400°C the two approaches yield equally good fits, suggesting that two state variables are not necessary. At higher temperatures, the two state variable approach provides a slightly better fit.

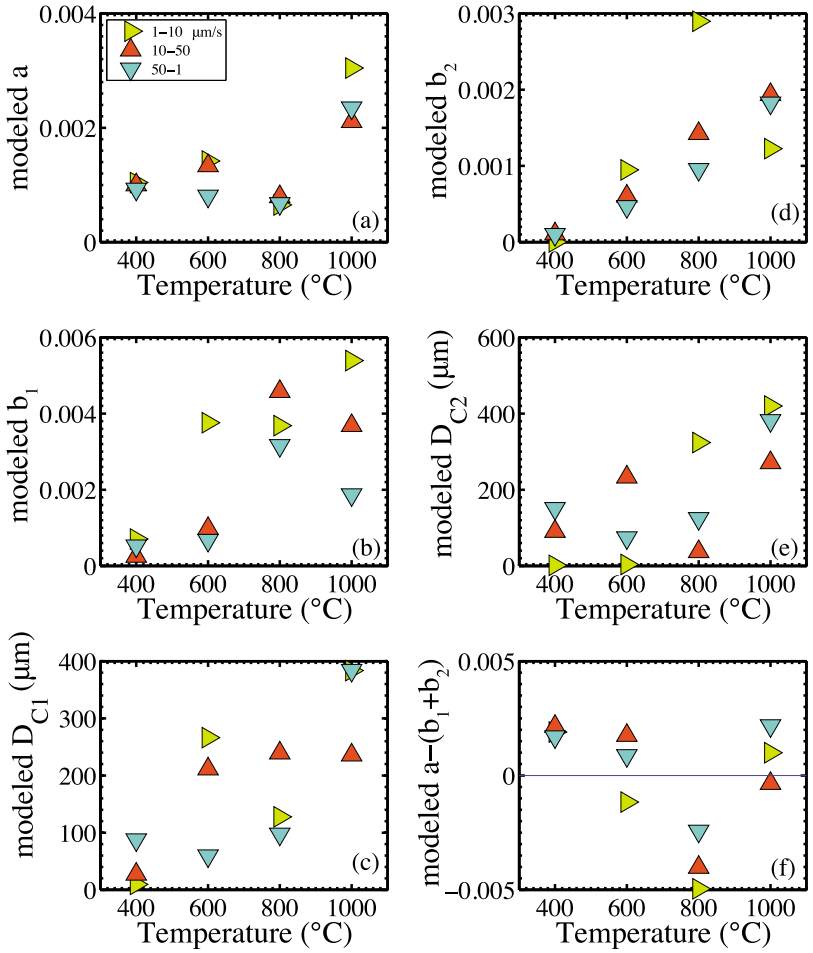

Figure 8. Plots of the parameters for the modeled fits in Figure 7 as a function of temperature. A two state variable approach was used with the state variable evolution law of *Ruina* [1983].

equally well. At higher temperatures, the two-mechanism model fits the data better. The parameters for the two state variable fits, shown in Figure 8, follow the same patterns as a function of temperature as observed with the one state variable approach. Similar to what can be observed in Figure 7, the magnitudes of b_1 and b_2 and of D_{C1} and D_{C2} are close to one another at lower temperatures. At higher temperatures D_{C1} and D_{C2} remain similar, but b_1 is greater than b_2. The improved fit to the data using two state variables, and the onset of the two state variable behavior at higher temperatures, suggests the possible onset of a second mechanism at higher temperatures.

3.5. Slide-Hold-Slide Tests

[26] To analyze the change in strength of the fault gouge when it is quasi-stationary, slide-hold-slide tests were performed after the velocity steps. Friction generally increases with hold time, indicating a type of restrengthening that is generally referred to as frictional healing [*Dieterich*, 1972; *Beeler et al.*, 1994]. Previous work shows that frictional healing is a function of temperature, shearing velocity, shear stress level, and chemical environment [*Karner et al.*, 1997; *Marone*, 1998b; *Karner and Marone*, 2001; *Frye and Marone*, 2002]. To measure the change in strength resulting from the holds, the overall linear trend of hardening or weakening with increasing displacement was removed from the data. In Figure 9, the relative change in friction coefficient is plotted as a function of slip displacement, determined by applying an elastic correction to measurements of load point displacement. During the holds, creep occurs within the gouge layer, which causes stress relaxation in the loading column. The loading actuator (outside the pressure vessel) is held stationary, but finite elastic stiffness of the elastic elements in the loading column results in displacement at the location of the axial LVDT (inside the pressure vessel). Thus, the gouge is not truly stationary during the hold. We follow the convention of measuring the frictional healing $\Delta\mu$ as the change in μ from immediately before the hold to the peak value following reloading after the hold (see annotation in Figure 10c). In Figure 10a, $\Delta\mu$ is plotted as a function of hold time for the four different temperatures investigated.

[27] The results from slide-hold-slide tests reveal a similar pattern of changes in mechanical behavior with temperature as the velocity step tests. The only sample with a positive values of $\Delta\mu$, and thus a peak in μ following the hold, is the sample deformed at 800°C. That sample displays increasing $\Delta\mu$ with increasing hold time. Samples deformed at all other temperatures show negative values of $\Delta\mu$, and thus do not strengthen during the holds. Instead maximum friction

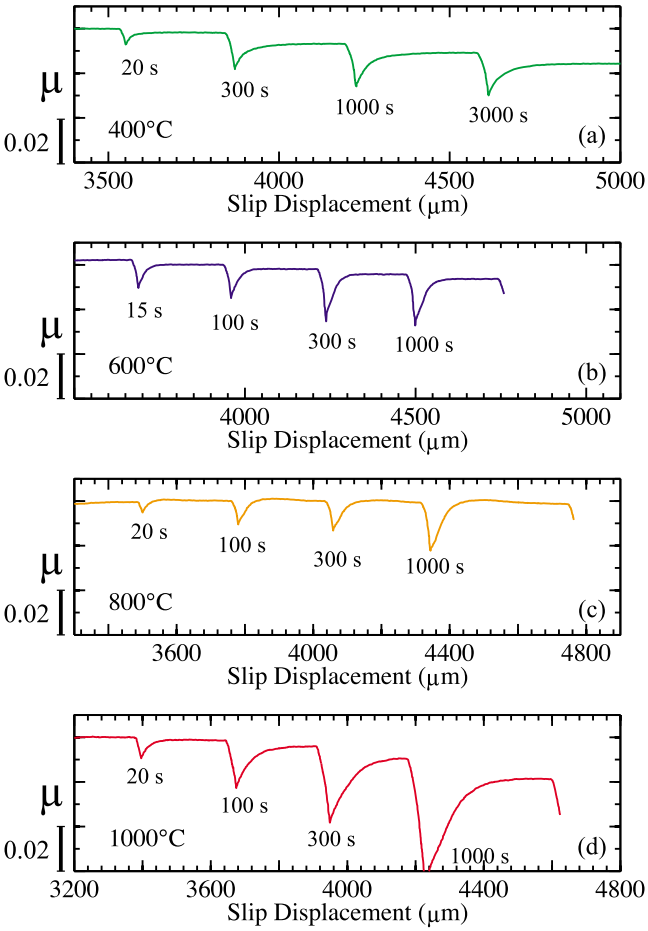

Figure 9. Plots of friction versus displacement for slide-hold-slide tests at each temperature. Note that sample creeps during holds and that steady state friction decreases after hold for all temperatures except 800°C.

following the hold decreases with increasing hold time. An example of the evolution of μ during a hold is shown in Figure 10c for the 300 s hold.

[28] The temperatures at which the gouge behaves in a velocity weakening manner during rate steps, for at least some velocities, are the temperatures at which $\Delta\mu$ is positive (800°C) or closest to neutral (600°C). Samples deformed at 1000°C are unique in that the drop in μ during the hold time is significantly greater than in samples deformed at lower temperatures.

3.6. Microstructural Observations

[29] Microstructural observations reveal information about the grain-scale processes accommodating deformation during shearing. The images presented in Figure 11 of thermally etched samples reveal the similarities and differences in grain morphology at the different temperatures investigated in this study. All of the samples display evidence of grain crushing with a fine-grained matrix making up most of the sample. Larger relict grains remain that do not form a load-bearing network across the thickness of the sample. The sample deformed at 400°C has the most clear evidence of comminution with highly angular grains and prevalent intragranular fractures. Few dislocations are present. The samples deformed

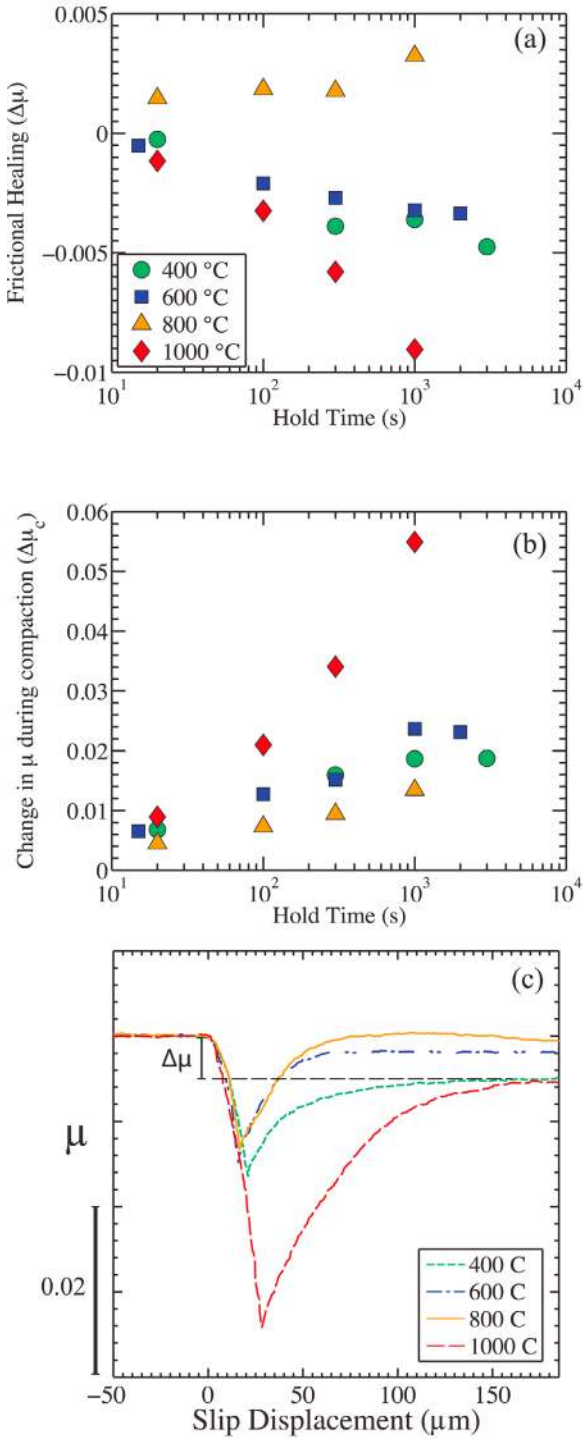

Figure 10. Data from slide-hold-slide tests at each temperature. (a) The frictional healing parameter ($\Delta\mu$) (see Figure 10c) is plotted versus log time. For all temperatures except 800°C, peak friction following a hold period is less than the initial steady state value and thus $\Delta\mu$ is negative. (b) Frictional creep during hold periods $\Delta\mu_c$ plotted versus log time. Creep is greatest at 1000°C. (c) Friction data for a 300 second hold at each temperature.

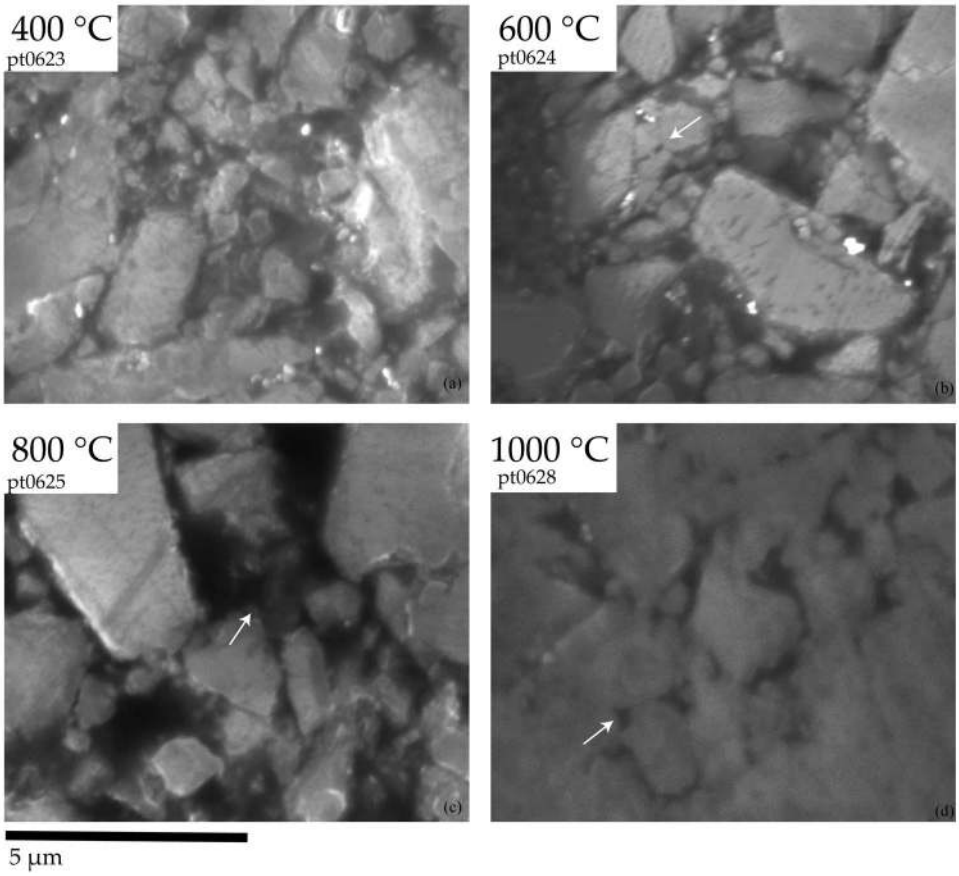

Figure 11. Secondary electron SEM images of samples impregnated in epoxy after deformation. All images are shown at the same scale. Note the similarity among samples deformed at 400, 600, and 800°C, with angular grains and significant epoxy filled void space. The arrow in Figure 11b indicates what appears to be a single grain that has been crushed to form multiple angular grains. The arrow in Figure 11c highlights an angular grain boundary adjacent to a large pore space. The sample deformed at 1000°C has less angular grains and less void space, which corresponds to greater contact area among grains. The arrow in Figure 11d indicates one of the more rounded grain boundaries and a much smaller intergranular void space what is typical in the samples deformed at lower temperatures.

at both 600 and 800°C have angular grains and evidence of grain crushing, with more prevalent grain fracturing at 600°C (Figure 11b). The image in Figure 12a shows evidence for grain fracturing and dislocation activity in the same grain. The grain appears to be crushed along the upper grain boundary with fractures associated with an asperity contact on that interface. The distribution of dislocations within the grain is heterogeneous with few dislocations near the fractured area and a greater dislocation density near other angular contacts where stress was concentrated. We observe dislocation densities around 9×10^{12} m^{-2} with a possible association of higher dislocation density with smaller grain size, perhaps indicating that smaller grains experience higher stress. The microstructural characteristics of the sample deformed at 1000°C are notably different from the samples deformed at lower temperatures. The grains are more rounded with flattened interfaces at grain contacts. The sample is more dense with less void space than the samples deformed at lower temperatures. These observations indicate that the average contact area of asperity junctions was larger at higher temperatures. In handling the samples, it was also apparent that the samples deformed at 1000°C were much less friable than samples deformed at lower temperatures, suggesting that the samples densified more during deformation at higher temperature.

4. Discussion

[30] In this study, the mechanical response of olivine fault gouge was observed to depend on temperature, pressure, sliding velocity (strain rate) and past slip history (frictional state or memory effect). Several lines of evidence indicate that the deformation was accommodated by macroscopically brittle processes, even at temperatures approaching the melting point of olivine. The yield stress was pressure dependent, microstructural observations indicate grain-scale fracturing, and the mechanical data are fit well by RSF laws. One of the goals of the experiments and analysis was to determine the interactions between this macroscopically brittle behavior and intragranular plastic deformation mechanisms (i.e. dislocation glide) at the asperity scale. In the following sections, we discuss the temperature dependent mechanisms that may control the strength of asperities, and we explore the effect of this temperature dependence on the rate and state friction

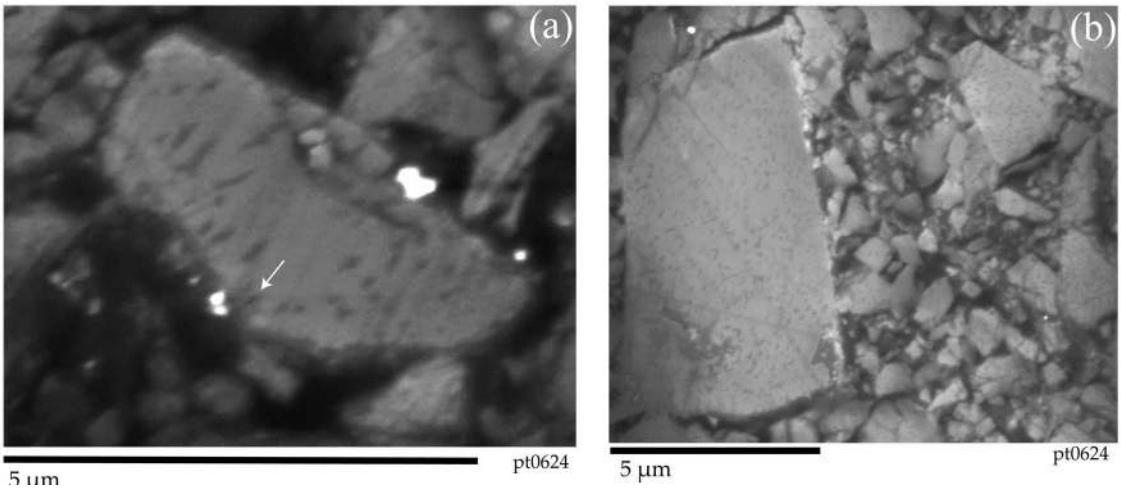

Figure 12. SEM images (secondary electron) of the sample deformed at 600°C. Dislocations appear as the dark patches within the grains in these decorated samples. Note the heterogeneous distribution of dislocations in Figure 12a, which we interpret as evidence for deformation accommodated by the motion of dislocations. The arrow in Figure 12a points to one angular grain boundary with higher dislocation density than observed in the center of the grain. The image in Figure 12b shows the wide range of grain sizes present within the sample. Dislocation density is greater in smaller grains, suggesting that the smaller grains experienced higher stress.

parameters (described earlier in section 2.1). The results provide insights into the physical mechanisms that underlie rate and state frictional behavior.

4.1. The Strength of Asperities

[31] Thermally activated plastic deformation mechanisms appear to play a role in determining the strength of contact asperities in our experiments. Microstructural observations reveal greater dislocation density near asperity contacts (Figure 12) suggesting that the motion of dislocations accommodated deformation at these contacts. Also, the yield strength of the gouge generally decreases with increasing temperature. This mechanical observation is consistent with a thermally activated process controlling some aspect of the strength of the gouge [*Rice et al.*, 2001].

[32] A fine grained aggregate can deform plastically by several different mechanisms, and the dominant (rate or stress controlling) mechanism depends on a number of parameters including: temperature, pressure, grain size, strain rate (or stress), and water fugacity. Dislocation glide accommodates deformation through the motion of dislocations, and is typically the dominant mechanism at low temperature and high stress. Dislocation glide is often referred to as low temperature plasticity to differentiate it from the higher temperature, lower stress mechanisms of dislocation climb, in which dislocations can "climb" over obstacles by vacancy diffusion (which occurs much faster at higher temperature), thus reducing the stress needed to propagate dislocation motion. Particularly in samples deformed at 600 and 800°C, in which a heterogenous distribution of dislocations was observed in thermally etched samples, we interpret dislocation glide to be the most likely plastic deformation mechanisms at asperity contacts. A flow law for dislocation glide in olivine was determined by indentation creep experiments on single crystals [*Goetze*, 1978; *Evans and Goetze*, 1979]. We use this flow law to determine the stress at asperities σ_A as a function of temperature T and strain rate $\dot{\varepsilon}$:

$$\sigma_A = \sigma_P \left[1 - \left(\frac{-RT}{H} \ln \frac{\dot{\varepsilon}}{B} \right)^{1/q} \right] \tag{5}$$

where the Peierl's stress σ_P = 8500 MPa, the gas constant $R = 8.314$ J/(mol K), the activation enthalpy $H = 5.4 \times 10^5$ J/mol, the empirical constant $B = 5.7 \times 10^{11}$ s^{-}1, and the exponent $q = 2$.

[33] Dislocation glide does not depend on grain size, so there is no grain size parameter in the flow law. However, as we observe in the microstructural images of the deformed samples, comminution during deformation causes dramatic grain size reduction. It is therefore important to consider the role of grain size sensitive mechanisms, particularly at the higher temperature end of the range explored in our experiments. Deformation mechanisms involving diffusion have a much stronger temperature dependence than dislocation glide, and they are highly grain size sensitive. Diffusion creep is well characterized by a power law creep flow law [e.g., *Hirth and Kohlstedt*, 2003], which can also be used to calculate σ_A:

$$\sigma_A = \left(\frac{\dot{\varepsilon} d^{-p} f\mathrm{H_2O}^r \exp\left(\frac{E+PV}{RT}\right)}{A} \right)^{1/n} \tag{6}$$

where d is the grain size, p = 3 is the grain size exponent, fH_2O is the water fugacity, r = 1 is the water fugacity exponent, E = 335 kJ/mol is the activation energy, P is the pressure, $V = 4\ 10^{-6}$m^3/mol is the activation volume, R is the gas constant, and T is the absolute temperature.

[34] In Figure 13, mechanical data are plotted from *Stesky et al.* [1974] (experiments were conducted at 400 MPa confining pressure), *Boettcher et al.* [2007] (100 MPa

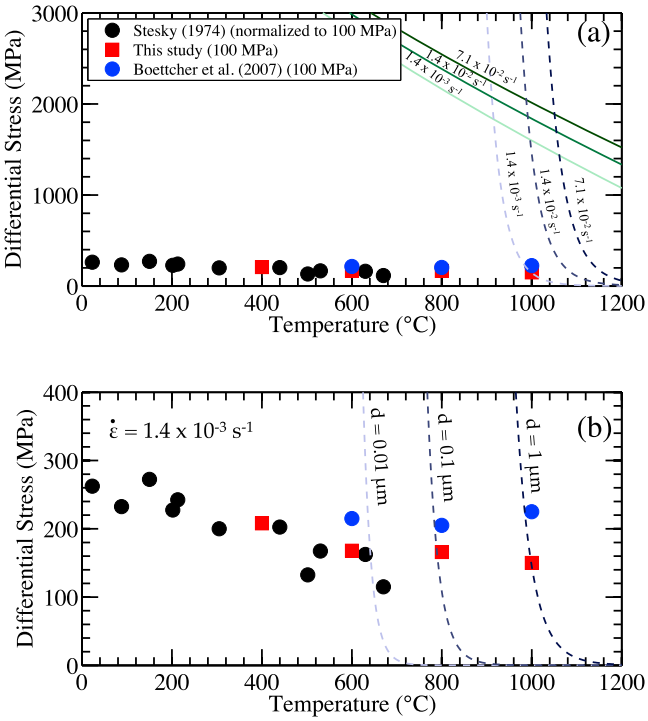

Figure 13. (a) A comparison of friction data and plastic flow laws on a plot of differential stress versus temperature [after *Hirth*, 2002]. Maximum differential stress data from *Stesky et al.* [1974] are from experiments conducted at 400 MPa confining pressure (normalized to 100 MPa for comparison), while those of *Boettcher et al.* [2007] and this study are from 100 MPa confining pressure. The Low temperature plasticity flow law of *Evans and Goetze* [1979] and the wet diffusion creep flow law of *Hirth and Kohlstedt* [2003] are plotted for the three strain rates corresponding to the strain rates at the three sliding velocities used in our study. (b) A plot of the grain size dependence of wet diffusion creep at a strain rate of $\dot{\varepsilon} = 1.4 \times 10^{-3}\ s^{-1}$.

confining pressure data), and this study (100 MPa confining pressure data). The data of *Stesky et al.* [1974] show a greater temperature dependence than *Boettcher et al.* [2007] or this study. This observation has been attributed to the possible presence of other phases, since the experiments were performed on natural dunite samples [*Hirth*, 2002]. However, the observed temperature dependence of frictional stress could also indicate the onset of plastic deformation mechanism and semi-brittle flow at lower temperatures with greater confining pressure, which would mean that the trend of the *Stesky et al.* [1974] data set indicates that the pressure sensitivity of strength diminishes with increasing temperature such that deformation is nearly pressure insensitive by 1000°C.

[35] Along with the mechanical data, Figure 13 shows the stress calculated from equations (5) and (6) as a function of temperature for the three different strain rates that correspond to the three different sliding velocities (1, 10 and 50 μm/s) used in our study. The strain rates were calculated assuming homogeneous deformation throughout the thickness of the sample. Because microstructural observations suggest that deformation is further localized into discrete deformation bands, the calculated strain rates are a lower bound. Comparison of the data with theory demonstrates that the stress of dislocation glide is significantly greater than the measured stress in the sample as a whole for all temperatures in our study. For dislocation glide to be active, stress must be concentrated at high stress asperity contacts. The comparison also demonstrates that above 1000°C, for the lowest strain rate explored in this study and the observed grain size of ~1 μm, the calculated stress is comparable to the measured stress. The grain size sensitivity of diffusion creep for a strain rate of $\dot{\varepsilon} = 1.4 \times 10^{-3}$ is presented in Figure 13b.

4.2. Asperity Contact Area

[36] Yielding at high stress asperities followed by creep causes an increase in the effective area of contact (often referred to as the "real" area of contact) A_R relative to the nominal area of the sample, A. A lower yield stress at the asperity results in greater amplification of A_R. Following the approach of *Tullis and Weeks* [1987], *Reinen et al.* [1994], and *Boettcher et al.* [2007], we can calculate the ratio of A_R/A by the following relation:

$$\frac{A_R}{A} = \frac{\sigma_1 - \sigma_3}{\sigma_A}, \tag{7}$$

where σ_A is calculated from equations (5) and (6). The results of this calculation for a grain size of 1 μm and a strain rate of $\dot{\varepsilon} = 1.4 \times 10^{-3}\ s^{-1}$ (the estimated minimum strain rate at our intermediate rate of 10 μm/s) are plotted in Figure 14 as a function of temperature.

[37] For the temperature range over which dislocation glide is the weaker deformation mechanism, the effective area of contact ranges from ~0.05–0.1. These values are typical for a wide range of materials [*Archard*, 1957; *Greenwood and Williamson*, 1966]. With the onset of diffusion creep at ~1000°C, the ratio of A_R/A increases dramatically.

[38] The calculated asperity contact area can be related to the modeled rate and state friction parameters. The D_C parameter is interpreted to be the slip distance necessary to

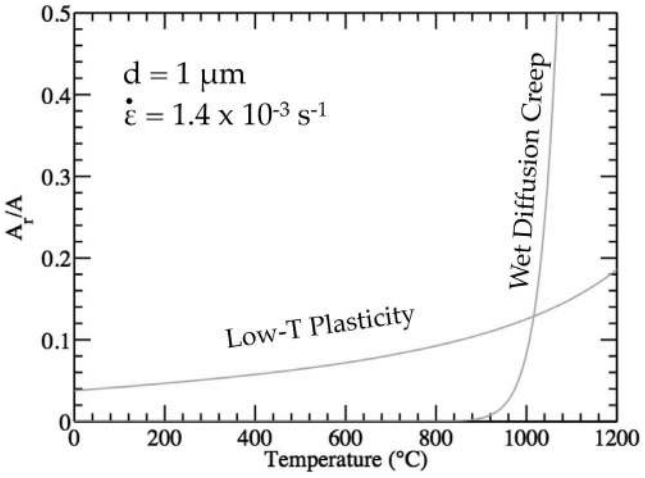

Figure 14. The effective contact area A_R/A as a function of temperature using the plastic flow laws to calculate asperity strength in equation (7). Note the dramatic increase in effective contact area at the onset of diffusion creep at around 1000°C for this grain size and strain rate.

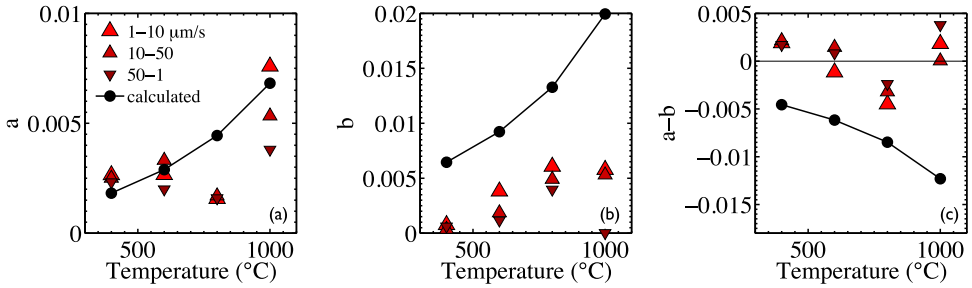

Figure 15. Comparison of the friction parameters obtained from our data (e.g., Figure 6) and the theoretical value of (a) parameter a using equation (9) with an activation volume of $\Omega = 1.4 \times 10^{-27}$ m^3, (b) theoretical value of parameter b as described in the text, and (c) theoretical value of $a - b$.

renew grain contacts. Increasing asperity contact area should correspond to a longer D_C. Our results demonstrate that D_C increases with increasing temperature (Figure 6b).

4.3. Effect of Temperature on the Direct Effect and Evolution Effect

[39] While initially introduced as an empirical parameter [e.g., *Dieterich*, 1979; *Ruina*, 1983], the $a\ln(V/V^*)$ term of equation (4) is widely interpreted to arise from a thermally activated process at asperity contacts for a broad range of materials and conditions [e.g., *Chester*, 1995; *Baumberger and Berthoud*, 1999; *Rice et al.*, 2001; *Nakatani*, 2001; *Beeler et al.*, 2007]. The general form of such a process is:

$$V = V_1 \exp\left(\frac{-E}{k_B T}\right), \tag{8}$$

where V is the sliding velocity, T is temperature, and $k_B = 1.38 \times 10^{-23}$ m^{2}kg/s^{2}K is Boltzman's constant. The activation energy has the form $E = E' - \tau_A \Omega$ in which $\tau_A = \mu\sigma_A$ is the average shear stress at asperity contacts and Ω is the activation volume. V_1 is not an arbitrary velocity, but can be regarded as a frequency of attempts over an activation barrier times a slip distance per successful attempt [*Rice et al.*, 2001]. By substituting equation (8) into equation (4) and rearranging, a theoretical formulation for the a parameter, such as that presented by *Baumberger and Berthoud* [1999], can be derived:

$$a = \frac{k_B T}{\sigma_A \Omega}. \tag{9}$$

In an analysis of previously published data, *Beeler et al.* [2007] used a normalization scheme to compare measurements of the rate and state a parameter with experimental data for low temperature plasticity and sub-critical crack growth, which are two common interpretations for the physical basis of the direct effect. The authors found that this form of the a parameter based on dislocation glide compared favorably with results from frictional sliding experiments.

[40] As plotted in Figure 15, this theory matches the trend of our data for an activation volume of $\Omega = 1.4 \times 10^{-27}$ m^3 (close to ten times the molecular volume for olivine). This activation volume is somewhat greater than was required to fit the data of *Boettcher et al.* [2007] in a similar analysis, where $\Omega = 5 \times 10^{-28}$ m^3 (approximately twice the molecular volume of olivine). This similarity in both studies is an encouraging result. However, *Boettcher et al.* [2007] correctly point out that Ω is not the same activation volume that describes the effects of pressure on kinetic processes, and it should not necessarily be equivalent to the molecular volume of the material. The exponent $q = 2$ in equation (5) captures an important strain rate dependence of the asperity stress that is not captured in equation (8) used to determine the theoretical a parameter.

[41] The evolution effect may also have a physical basis in the creep properties of asperities, making it possible to use the flow laws to constrain the b parameter. In their analysis of rate and state friction, *Baumberger and Berthoud* [1999] show that $b \approx \mu_0/n$, where μ_0 is the coefficient of friction prior to the velocity step and n is the power law exponent in the flow law $\dot{\varepsilon} \propto \sigma^n$. The interpreted creep mechanism at asperities in this study is not a power law mechanism, which may detract from the applicability of this theory, but we can calculate an effective value of the stress exponent from equation (5). A comparison of the calculated b parameter and the measured values of b is plotted in Figure 15b. Consistent with the calculation, the measured values of b increase with increasing temperature, but the calculated values are consistently greater than the measured values.

4.4. Mechanistic Interpretation for Temperature Dependence of Frictional Sliding Stability

[42] The results of our experiments demonstrate two transitions in frictional stability with increasing temperature. The higher temperature transition from velocity weakening to velocity strengthening between 800 and 1000°C supports the results of *Boettcher et al.* [2007]. In this study, we explored a broader temperature range than *Boettcher et al.* [2007], and the transition from velocity strengthening to conditionally velocity weakening between 400 and 600°C is a new result. This result is supported by the work of *Stesky et al.* [1974], in which olivine friction was investigated up to temperatures of ~600°C. Stesky reported stable sliding within the entire temperature range investigated, which is consistent with a velocity strengthening regime.

[43] Our analysis and observations suggest that the higher temperature transition may be related to the onset of diffusion creep within the fine grained fault gouge, which promotes rapid densification and corresponding increase in contact area. This interpretation is consistent with the large jump in D_C between 800 and 1000°C for the rate step with the slowest velocity after the rate step (Figures 6c and 6e). This explanation could apply to studies on other materials

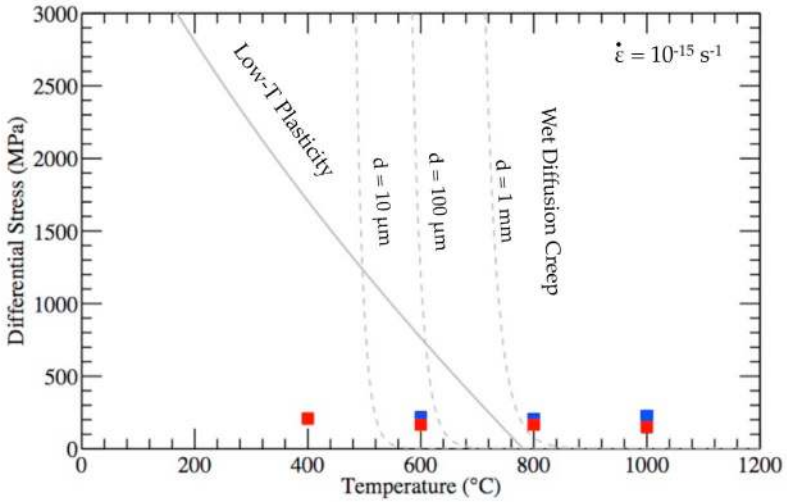

Figure 16. Plot similar to Figure 13b but extrapolated to a range of grain sizes appropriate for the upper mantle and to a strain rate of 10^{-15} s^{-1}. This plot shows the expected onset of diffusion creep at temperatures consistent with the transition from velocity weakening to velocity strengthening behavior.

with a similar transition in sliding stability with temperature. In the experiments of *Blanpied et al.* [1995], the transition from velocity weakening to velocity strengthening is observed in wet granite gouge at around 300°C, which is an appropriate temperature for diffusion creep to initiate at the strain rates in the experiment [*van Noort et al.*, 2008; *van Noort and Spiers*, 2009]. Notably, the transition is not observed in dry granite gouge, which should require a higher temperature for the activation of creep mechanisms.

[44] A mechanistic interpretation for the lower temperature transition in sliding stability may lie simply in the different dependence of a and b on temperature (black line in Figure 15). While the existing theory for the b parameter, described above, does not fit the magnitude of the data well, it does capture the trend of increasing value of b with increasing temperature. The frictional stability parameter ($a - b$) is predicted to be increasingly velocity weakening with increasing temperature. The over-prediction of b from theory may result from uncertainties in the relationship between stress and strain rate at these conditions [*Boettcher et al.*, 2007].

[45] The higher temperature switch from velocity weakening to velocity strengthening between 800 and 1000°C observed in the data is a divergence from the trend described above and presented in Figure 15, which would predict increasingly velocity weakening behavior with increasing temperature. This higher temperature switch is more difficult to explain within this theoretical framework. With $b \approx \mu_0/n$, the only way to significantly decrease b is to significantly increase tn. We are not aware of a physically meaningful mechanism for a large increase in n relative to low temperature plasticity. Our microstructural observations and our analysis of flow laws suggest an increasing importance of diffusion creep in this temperature range. Because $n = 1$ for diffusion creep, this mechanism switch does not solve the problem described above. Thus, our observations suggest that this theoretical framework for b does not capture some important aspects of the temperature dependence of deformation. Perhaps as the grain contact area increases dramatically (as predicted in this temperature range in the analysis of Figure 14) and viscous flow becomes a more important component of deformation, the apparent power law exponent framework for b no longer holds.

4.5. Implications

[46] By assuming that the transition from velocity weakening to velocity strengthening behavior is related to the stress at the asperity contacts, *Boettcher et al.* [2007] extrapolated the laboratory results to constrain the temperature of the transition in Earth to be ~600°C. This extrapolation is in excellent agreement with observations of the depth extent of seismicity [*Sibson*, 1984; *Abercrombie and Ekstrom*, 2001]. The analysis here provides a mechanistic interpretation for this transition from velocity weakening to velocity strengthening, which we interpret to be the onset of diffusion creep in accommodating deformation at high stress asperities. In Figure 16, the flow laws for low temperature plasticity and diffusion creep are plotted for a range of grain sizes appropriate for the upper mantle and a strain rate of 10^{-15} s^{-1}. For these conditions, the stress for diffusion creep becomes weaker than that of low temperature plasticity around 550–800°C, thus supporting the interpretation that changing deformation mechanisms at asperity contacts may control sliding stability.

Table 1. Experimental Details

Sample	Temperature (°C)	Piston Angle	P_c (MPa)
PT0602	800	30°	100
PT0603	1000	30°	100
PT0604	600	30°	100
PT0606	400	30°	100
PT0623	400	45°	100
PT0624	600	45°	100
PT0625	800	45°	100
PT0626	600	45°	50
PT0627	600	45°	150
PT0628	1000	45°	100
PT0636[a]	800	45°	100

[a]Alumina piston.

Table 2. Model Results

Sample	Temperature (°C)	Rate	a	b	D_C
PT0623	400	1–10	0.002649	0.000754	8.983
		10–50	0.002504	0.000354	37.864
		50–1	0.002319	0.000615	92.110
PT0624	600	1–10	0.002656	0.003811	258.112
		10–50	0.003318	0.001865	298.865
		50–1	0.001995	0.001163	72.529
PT0625	800	1–10	0.001565	0.006066	169.897
		10–50	0.001699	0.004903	134.303
		50–1	0.001592	0.003973	103.351
PT0628	1000	1–10	0.007590	0.005771	326.481
		10–50	0.005334	0.005303	215.715
		50–1	0.0038	0.00002	180

Sample	Temperature (°C)	Rate	a	b_1	D_{C1}	b_2	D_{C2}
PT0623	400	1–10	0.002603	0.000705	9.56	0.000002	1.5
		10–50	0.002502	0.000251	27.279	0.000107	90.534
		50–1	0.002318	0.000525	87.596	0.000100	150.794
PT0624	600	1–10	0.003545	0.003760	266.341	0.000948	3.789
		10–50	0.003339	0.000981	211.435	0.000603	233.224
		50–1	0.002011	0.000674	59.463	0.000467	73.822
PT0625	800	1–10	0.001625	0.003682	127.682	0.002898	323.779
		10–50	0.001987	0.004579	239.230	0.001425	37.314
		50–1	0.001684	0.003162	97.578	0.000953	124.312
PT0628	1000	1–10	0.007614	0.005390	383.556	0.001226	419.861
		10–50	0.005271	0.003685	235.743	0.001936	270.896
		50–1	0.005873	0.001868	384.063	0.001825	381.505

[47] A similar variation in sliding stability with temperature with velocity strengthening at low and high temperatures and velocity weakening at intermediate temperatures has been observed in other materials [*Blanpied et al.*, 1995; *He et al.*, 2007; *Tembe et al.*, 2009; *den Hartog et al.*, 2012]. Additionally, experimental studies have found that in some settings, the weakening predicted from mineral alteration is not enough to explain geological observations, and thermally activated dissolution-precipitation creep processes may be important to consider [*Smith and Faulkner*, 2010]. This work supports the interpretation that this temperature dependence can be understood through relating the RSF parameters to plastic deformation at asperity contacts. All of these materials are weaker than olivine, and have lower activation energies for plastic deformation, so the lower temperatures at which the stability transition is observed is consistent with the interpreted role of plastic deformation.

5. Conclusions

[48] We observe multiple transitions in frictional sliding stability with temperature in sheared layers of fine grained olivine gouge. These transitions can be understood through the role of plastic deformation at asperity contacts. The material becomes increasingly velocity weakening with increasing temperature within the temperature range that dislocation glide is the dominant yielding mechanism at asperities. At higher temperatures, with dependence upon grain size and strain rate, diffusion creep processes can weaken the asperity contacts leading to increased contact area and densification. These transitions in sliding stability observed in laboratory experiments can be extrapolated to upper mantle conditions and are consistent with observations of the depth extent of seismicity along oceanic transform faults (Tables 1 and 2).

[49] **Acknowledgments.** This material is based upon work supported by the National Science Foundation Award EAR-0948246 (to DSHK) as well as EAR-0950517 and EAR-0911569 (to CM). We thank David Kohlstedt for allowing the use of laboratory facilities supported by the National Science Foundation Award EAR-1214876. We also thank Y. Bernabe, L. Montesi, and an anonymous reviewer for critical comments that improved the paper.

References

Abercrombie, R., and G. Ekstrom (2001), Earthquake slip on oceanic transform faults, *Nature*, *410*(6824), 74–77.

Archard, J. (1957), Elastic deformation and the laws of friction, *Proc. R. Soc. London, Series A*, *243*(1233), 190–205.

Baumberger, T., and P. Berthoud (1999), Physical analysis of the state- and rate-dependent friction law. II. Dynamic friction, *Phys. Rev. B*, *60*(6), 3928–3939.

Bayart, E., A. Rubin, and C. Marone, (2006), Evolution of fault friction following large velocity jumps, *Eos Trans. AGU*, *87*(52), Fall Meet. Suppl., Abstract S31A-0180.

Beeler, N., T. E. Tullis, and J. Weeks (1994), The roles of time and displacement in the evolution dffect in rock friction, *Geophys. Res. Lett.*, *21*(18), 1987–1990.

Beeler, N. M., T. E. Tullis, A. K. Kronenberg, and L. A. Reinen (2007), The instantaneous rate dependence in low temperature laboratory rock friction and rock deformation experiments, *J. Geophys. Res.*, *112*, B07310, doi:10.1029/2005JB003772.

Blanpied, M., D. Lockner, and J. Byerlee (1995), Frictional slip of granite at hydrothermal conditions, *J. Geophys. Res.*, *100*(B7), 13,045–13,064.

Boettcher, M. S., G. Hirth, and B. Evans (2007), Olivine friction at the base of oceanic seismogenic zones, *J. Geophys. Res.*, *112*, B01205, doi:10.1029/2006JB004301.

Bos, B., and C. Spiers (2000), Effect of phyllosilicates on fluid-assisted healing of gouge-bearing faults, *Earth Planet. Sci. Lett.*, *184*(1), 199–210.

Brace, W., and D. L. Kohlstedt (1980), Limits on lithospheric stress imposed by laboratory experiments, *J. Geophys. Res.*, *85*, 6248–6252.

Byerlee, J. (1978), Friction of rocks, *Pure Appl. Geophys.*, *116*, 615–627.

Chester, F. (1995), A rheologic model for wet crust applied to strike-slip faults, *J. Geophys. Res.*, *100*, 13,033–13,044.

Chester, F., and N. Higgs (1992), Multimechanism friction constitutive model for ultrafine quartz gouge at hypocentral conditions, *J. Geophys. Res.*, *97*(B2), 1859–1870.

den Hartog, S. A. M., C. J. Peach, D. A. M. de Winter, C. J. Spiers, and T. Shimamoto (2012), Frictional properties of megathrust fault gouges at low sliding velocities: New data on effects of normal stress and temperature, *J. Struct. Geol.*, *38*, 156–171.

Dieterich, J. (1972), Time-dependent friction as a possible mechanism for aftershocks, *J. Geophys. Res.*, *77*, 3771–3781.

Dieterich, J. (1979), Modeling of rock friction: 1. Experimental results and constitutive equations, *J. Geophys. Res.*, *84*(B5), 2161–2170.

Escartin, J., G. Hirth, and B. Evans (1997), Effects of serpentinization on the lithospheric strength and the style of normal faulting at slow-spreading ridges, *Earth Planet. Sci. Lett.*, *151*(3–4), 181–189.

Escartin, J., G. Hirth, and B. Evans (2001), Strength of slightly serpentinized peridotites: Implications for the tectonics of oceanic lithosphere, *Geology*, *29*(11), 1023–1026.

Evans, B., and C. Goetze (1979), The temperature variation of hardness of olivine and its implications for polycrystalline yield stress, *J. Geophys. Res.*, *84*(B10), 5505–5524.

Frye, K. M., and C. Marone (2002), Effect of humidity on granular friction at room temperature, *J. Geophys. Res.*, *107*(B11), 2309, doi:10.1029/2001JB000654.

Goetze, C. (1978), Mechanisms of creep in olivine, *Philos. Trans. R. Soc. London, Ser. A*, *288*, 99–119.

Greenwood, J., and J. Williamson (1966), Contact of nominally flat surfaces, *Proc. R. Soc. London, Ser. A*, *295*(1442), 300–319.

He, C., Z. Wang, and W. Yao (2007), Frictional sliding of gabbro gouge under hydrothermal conditions, *Tectonophysics*, *445*(3–4), 353–362.

Heslot, F., T. Baumberger, B. Perrin, B. Caroli, and C. Caroli (1994), Creep, stick-slip, and dry-friction dynamics—Experiments and a heuristic model, *Phys. Rev. E*, *49*(6), 4973–4988.

Hirth, G. (2002), Laboratory constraints on the rheology of the upper mantle, in *Reviews in Mineralogy and Geochemistry*, edited by S.-Y. Karato and H.-R. Wenk, pp. 97–120, Mineral. Soc. of Am., Washington, D. C.

Hirth, G., and D. L. Kohlstedt (2003), Rheology of the upper mantle and the mantle wedge: A view from the experimentalists, in *Inside the Subduction Factory*, *Geophys. Monogr. Ser.*, vol. 138, pp. 83–105, AGU, Washington, D. C.

Hobbs, B. E., H. Muhlhaus, and A. Ord (1990), Instability, softening and localization of deformation, *Geol. Soc. Spec. Publ.*, *54*, 143–165.

Karner, S., and C. Marone (2001), Frictional restrengthening in simulated fault gouge: Effect of shear load perturbations, *J. Geophys. Res.*, *106*(B9), 19,319–19,337.

Karner, S., C. Marone, and B. Evans (1997), Laboratory study of fault healing and lithification in simulated fault gouge under hydrothermal conditions, *Tectonophysics*, *277*, 41–55.

Kohlstedt, D. L., C. Goetze, W. B. Durham, and J. Sande (1976), New technique for decorating dislocations in olivine, *Science*, *191*, 1045–1046.

Kohlstedt, D. L., B. Evans, and S. J. Mackwell (1995), Strength of the lithosphere: Constraints imposed by laboratory experiments, *J. Geophys. Res.*, *100*(B9), 17,587–17,602.

Li, Q., T. E. Tullis, D. Goldsby, and R. W. Carpick (2011), Frictional ageing from interfacial bonding and the origins of rate and state friction, *Nature*, *480*(7376), 233–236.

Marone, C. (1998a), Laboratory-derived friction laws and their application to seismic faulting, *Annu. Rev. Earth Planet. Sci.*, *26*(1), 643–696.

Marone, C. (1998b), The effect of loading rate on static friction and the rate of fault healing during the earthquake cycle, *Nature*, *391*, 69–72.

Marone, C., and B. Kilgore (1993), Scaling of the critical slip distance for seismic faulting with shear strain in fault zones, *Nature*, *362*(6421), 618–621.

Marone, C., and C. Scholz (1988), The depth of seismic faulting and the upper transition from stable to unstable slip regimes, *Geophys. Res. Lett.*, *15*(6), 621–624.

Marone, C., M. Cocco, E. Richardson, and E. Tinti (2009), The critical slip distance for seismic and aseismic fault zones of finite width, in *Fault-Zone Properties and Earthquake Rupture Dynamics*, edited by E. Fukuyama, pp. 135–162, Elsevier, New York.

Montesi, L. G. J., and M. T. Zuber (2002), A unified description of localization for application to large-scale tectonics, *J. Geophys. Res.*, *107*(B3), 2045, doi:10.1029/2001JB000465.

Moore, D. E., and D. A. Lockner (2008), Talc friction in the temperature range 25 degrees–400 degrees C: Relevance for fault-zone weakening, *Tectonophysics*, *449*, 120–132.

Nakatani, M. (2001), Conceptual and physical clarification of rate and state friction: Frictional sliding as a thermally activated rheology, *J. Geophys. Res.*, *106*(B7), 13,347–13,380.

Niemeijer, A. R., and C. J. Spiers (2006), Velocity dependence of strength and healing behaviour in simulated phyllosilicate-bearing fault gouge, *Tectonophysics* , *427* , 231–253.

Paterson, M. S. (1990), Rock deformation experimentation, in *The Brittle-Ductile Transition in Rocks: The Heard Volume*, *Geophys. Monogr. Ser.*, vol. 56, edited by A. G. Duba et al., pp. 187–194, AGU, Washington, D. C.

Reinen, L. A., T. E. Tullis, and J. Weeks, J. (1992), Two-mechanism model for frictional sliding of serpentinite, *Geophys. Res. Lett.*, *19*(15), 1535–1538.

Reinen, L. A., J. Weeks, and T. E. Tullis (1994), The frictional behavior of lizardite and antigorite serpentinites: Experiments, constitutive models, and implications for natural faults, *Pure Appl. Geophys.*, *143*(1/2/3), 317–358.

Rice, J. R., and A. L. Ruina (1983), Stability of steady frictional slipping, *J. Appl. Mech.*, *50*(2), 343–349.

Rice, J. R., N. Lapusta, and K. Ranjith (2001), Rate and state dependent friction and the stability of sliding between elastically deformable solids, *J. Mech. Phys. Solids*, *49*(9), 1865–1898.

Ruina, A. (1983), Slip instability and state variable friction laws, *J. Geophys. Res.*, *88*(B12), 10,359–10,370.

Scholz, C. (1998), Earthquakes and friction laws, *Nature*, *391*, 37–42.

Shimamoto, T. (1986), Transition between frictional slip and ductile flow for halite shear zones at room temperature, *Science*, *231*(4739), 711–714.

Sibson, R. H. (1984), Roughness at the base of the seismogenic zone: Contributing factors, *J. Geophys. Res.*, *89*(B7), 5791–5799.

Sleep, N. (1997), Application of a unified rate and state friction theory to the mechanics of fault zones with strain localization, *J. Geophys. Res.*, *102*(B2), 2875–2895.

Smith, S. A. F., and D. R. Faulkner (2010), Laboratory measurements of the frictional properties of the Zuccale low-angle normal fault, Elba Island, Italy, *J. Geophys. Res.*, *115*, B02407, doi:10.1029/2008JB006274.

Stesky, R., W. Brace, and D. Riley (1974), Friction in faulted rock at high temperature and pressure, *Tectonophysics*, *23*, 177–203.

Stesky, R. M. (1978), Rock friction-effect of confining pressure, temperature, and pore pressure, *Pure Appl. Geophys.*, *116*(4–5), 690–704.

Tembe, S., D. Lockner, and T.-F. Wong (2009), Constraints on the stress state of the San Andreas Fault with analysis based on core and cuttings from San Andreas Fault Observatory at Depth (SAFOD) drilling phases 1 and 2, *J. Geophys. Res.*, *114*, B11401, doi:10.1029/2008JB005883.

Tenthorey, E., and S. F. Cox (2006), Cohesive strengthening of fault zones during the interseismic period: An experimental study, *J. Geophys. Res.*, *111*, B09202, doi:10.1029/2005JB004122.

Tenthorey, E., C. Scholz, E. Aharonov, and A. Leger (1998), Precipitation sealing and diagenesis: 1. Experimental results, *J. Geophys. Res.*, *103*, 23,951–23,967.

Tullis, T. E., and J. Weeks (1987), Micromechanics of frictional resistance of calcite, *Eos Trans. AGU*, *68*, 405.

van Noort, R., and C. J. Spiers (2009), Kinetic effects of microscale plasticity at grain boundaries during pressure solution, *J. Geophys. Res.*, *114*, B03206, doi:10.1029/2008JB005634.

van Noort, R., C. J. Spiers, and G. M. Pennock (2008), Compaction of granular quartz under hydrothermal conditions: Controlling mechanisms and grain boundary processes, *J. Geophys. Res.*, *113*, B12206, doi:10.1029/2008JB005815.